Field and Bench Test Evaluation of Range Extension Control System for Electric Vehicles Based on Front and Rear Driving-Braking Force Distributions

Hiroshi Fujimoto and Shingo Harada
The University of Tokyo
5-1-5, Kashiwanoha, Kashiwa, Chiba, Japan
fujimoto@k.u-tokyo.ac.jp
Koji Sato and Yusuke Matsuo
Ono Sokki Co.,Ltd.
1-16-1, Hakusan-midoriku, Yokohama, Kanagawa, Japan

Yuichi Goto and Daisuke Kawano
National Traffic Safety and Environment Laboratory
7-42-27, Jindaiji-higashimachi, Chofu, Tokyo, Japan

***Abstract*—Electric vehicles (EVs) have a disadvantage in that the cruising distance per charge is short. This paper proposes a model-based range extension control system (RECS) for EVs. The proposed system optimizes the front and rear driving-braking force distributions by considering the slip ratio of the wheels and the motor loss. The optimal distribution depends solely on the vehicle acceleration and velocity. Therefore, this system is effective not only at constant speeds but also in acceleration and deceleration modes. Bench tests were conducted for more precise evaluation and to realize experimental results with high reproducibility. The effectiveness of the proposed system was verified through field and bench tests.**

***Keywords*—bench test, driving and braking force distribution, electric vehicle, range extension control system**

I. Introduction

Nowadays, EVs are receiving attention because of environmental concerns such as global warming, exhaustion of fossil fuels, and air pollution. In addition, EVs have remarkable advantages in motion control compared with internal combustion engine vehicles (ICEVs) [1]:

1) The response to the driving-braking force by the motor is much faster than that of engines (about 100 times).
2) Development of in-wheel motors enables the individual control of each wheel.
3) The generated torque can be measured precisely from the motor current.
4) Smooth braking torque can be generated by regeneration.

Research is actively ongoing on traction control [2], [3] and stability control [4], [5] to utilize the above advantages.

One reason that is preventing EVs from spreading is that its mileage per charge is shorter than that of conventional ICEVs. In order to solve this problem, wireless power transfer for moving vehicles [6], [7], [8] is being researched. As another approach, ultracapacitors are being utilized for energy storage systems to improve the energy regeneration [9], [10], [11]. Research is also being carried out to improve the efficiency of motors [12]. In order to realize high-efficiency motor control, Inoue et al. examined torque and angular velocity patterns that maximize efficiency during acceleration and deceleration [13]. Yuan and Wang utilized the independent characteristics of traction motors to develop a torque distribution method for decreasing EV energy consumption where two motors with the same efficiency characteristics are used [14].

The authors' research group previously proposed the range extension control system (RECSs) [15], [16], which does not involve changes to the vehicle structure such as an additional clutch [14] or the motor type. Instead, the RECS extends the cruising range of a vehicle by motion control. Previously, the RECS was evaluated in terms of the acceleration and deceleration on a straight road [17]. The effectiveness of the proposed system was only verified for operation at low speeds. It has not been verified for operation at high speeds, where the ratios of the driving resistance and motor iron loss to the total loss are relatively large. Therefore, experiments on operation at high speeds are necessary for more appropriate evaluation of the RECS. In this study, a bench test was performed to realize high reproducibility of the results along with a field test to evaluate the proposed system [16]. The effectiveness of the proposed system was verified through the field and bench tests.

II. Experimental Vehicle and Vehicle Model

A. Experimental Vehicle

This study used the original electric vehicle "FPEV–2 Kanon," which was developed in-house. This vehicle has four outer rotor–type in-wheel motors. Since these are direct drive–type motors, the reaction force from the

(a) FPEV–2 Kanon.

(b) dSPACE AutoBox.

(c) Front motor.

(d) Rear motor.

Fig. 1. Experimental vehicle.

TABLE I. VEHICLE SPECIFICATIONS.

Vehicle mass M	854 kg
Wheelbase l	1.715 m
Distance from CG to front/rear axles l_f, l_r	l_f:1.013 m l_r:0.702 m
Gravity height h_g	0.51 m
Front wheel inertia J_{ω_f}	1.24 Nms^2
Rear wheel inertia J_{ω_r}	1.26 Nms^2
Wheel radius r	0.302 m

road is directly transferred to the motor without backlash from the reduction gear.

Fig. 1 shows the experimental vehicle. The dSPACE AutoBox (DS1103) was used for real-time data acquisition and control. Table I and Table II show the specifications of the vehicle and in-wheel motors. Fig. 2 presents the efficiency map of the front and rear in-wheel motors. In this study, higher torque operation points where the motor torque was greater than one and half times the rated torque were not used for the evaluation. Since the front and rear motors installed in the vehicle were different, their efficiency maps were also different. Therefore, the cruising range can be extended by employing the difference in efficiency.

Fig. 3 illustrates the power system of the vehicle. A lithium-ion battery was used as the power source. The voltage of the main battery was 160 V (ten battery modules were connected in series). The voltage was boosted to 320 V by a chopper. In this study, the chopper loss was not evaluated because it was independent of the torque distribution.

TABLE II. SPECIFICATIONS OF IN-WHEEL MOTORS.

	Front	Rear
Manufacturer	TOYO DENKI SEIZO K.K.	
Type	Direct drive system Outer rotor type	
Rated torque	110 Nm	137 Nm
Maximum torque	500 Nm	340 Nm
Rated power	6.0 kW	4.3 kW
Maximum power	20.0 kW	10.7 kW
Rated speed	382 rpm	300 rpm
Maximum speed	1113 rpm	1500 rpm

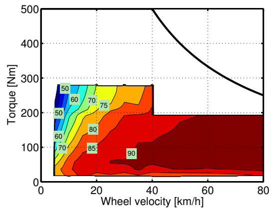

(a) Front motor.

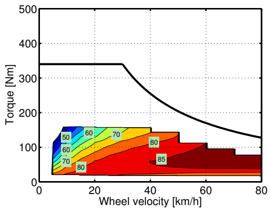

(b) Rear motor.

Fig. 2. Efficiency maps of front and rear motors.

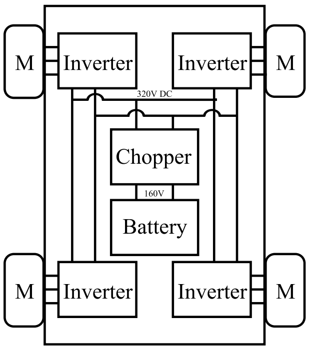

Fig. 3. Electric power system of vehicle.

B. Vehicle Model

The four wheel–drive vehicle model is described here. The wheel rotation is expressed by (1). For straight driving, the driving-braking forces of the right and left wheels are equal. Therefore, the vehicle dynamics is

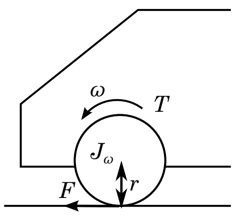

(a) Rotational motion of wheel

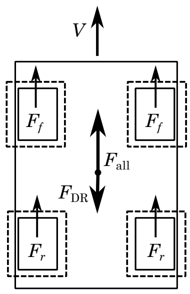

(b) Longitudinal motion of vehicle

Fig. 4. Vehicle model.

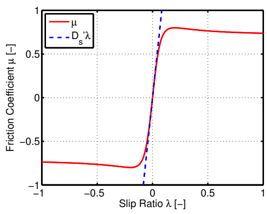

Fig. 5. Example of μ–λ curve.

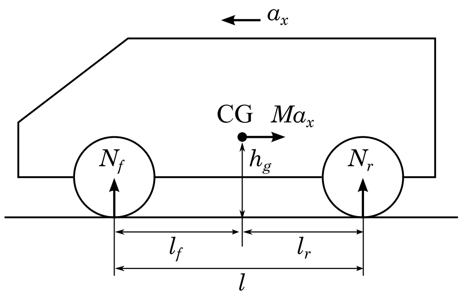

Fig. 6. Load transfer model.

expressed by (2) and (3).

$$J_{\omega_j}\dot{\omega}_j = T_j - rF_j, \tag{1}$$

$$M\dot{V} = F_{\mathrm{all}} - F_{\mathrm{DR}}, \tag{2}$$

$$F_{\mathrm{all}} = 2\sum_{j=f,r} F_j, \tag{3}$$

where ω_j is the wheel angular velocity, V is the vehicle speed, T_j is the motor torque, F_{all} is the total driving-braking force, F_j is the driving-braking force of each wheel, M is the vehicle mass, r is the wheel radius, J_{ω_j} is the wheel inertia, and F_{DR} is the driving resistance. The subscript j represents f or r (f stands for front, and r represents rear).

Next, the slip ratio λ_j is defined as

$$\lambda_j = \frac{V_{\omega_j} - V}{\max(V_{\omega_j}, V, \epsilon)}, \tag{4}$$

where $V_{\omega_j} = r\omega_j$ is the wheel speed and ϵ is a small constant to avoid zero division. $\lambda_j > 0$ means driving, and $\lambda_j < 0$ means braking. The slip ratio λ is known to be related with the coefficient of friction μ, as shown in Fig. 5 [18]. In region $|\lambda| \ll 1$, μ is nearly proportional to λ. By using the normal forces of each wheel N_j during longitudinal acceleration with a_x and the slope of the curve, the driving force of each tire is expressed as

$$F_j = \mu_j(\lambda_j)N_j(a_x) \approx D'_s\lambda_j N_j(a_x), \tag{5}$$

where D'_s is the normalized driving stiffness.

The normal forces of each wheel during the longitudinal acceleration process are calculated as follows:

$$N_f(a_x) = \frac{1}{2}\left(\frac{l_r}{l}Mg - \frac{h_g}{l}Ma_x\right), \tag{6}$$

$$N_r(a_x) = \frac{1}{2}\left(\frac{l_f}{l}Mg + \frac{h_g}{l}Ma_x\right), \tag{7}$$

where N_f and N_r are the front and rear normal forces, respectively, l_f and l_r are the distances from the center of gravity to the front and rear axles, respectively, and h_g is the height of the center of gravity. The acceleration direction is defined as positive when the vehicle is accelerating.

C. Driving-Braking Force Distribution Model

During straight driving, the required total driving-braking force can be distributed to each wheel. Since the EV motors were assumed to be independently controlled in this study, the driving-braking force distribution has an extra degree of freedom. By introducing the front and rear driving-braking force distribution ratio k, the driving-braking forces can be formulated based on the total driving-braking force F_{all} and the distribution ratio k as follows [16]:

$$F_j(k) = \frac{1}{2}\gamma_j(k)F_{\mathrm{all}}, \tag{8}$$

$$\gamma_j(k) = \begin{cases} 1-k & (j=f) \\ k & (j=r) \end{cases}. \tag{9}$$

The distribution ratio k varies from 0 to 1. $k = 0$ means that the vehicle is a front-driven system, and $k = 1$ means that it is rear-driven only. Note that, even if the driving force F_j is zero, the torque T_j is not always zero according to (1).

D. Modeling of Inverter Input Power

The slip ratio and motor loss can be considered to derive the distribution ratio that minimizes the inverter input power. Neglecting the inverter loss and mechanical loss of the motor, the inverter input power P_{in} is expressed as

$$P_{\mathrm{in}} = P_{\mathrm{out}} + P_c + P_i, \tag{10}$$

where P_{out} is the sum of the mechanical output of each motor, P_c is the sum of the copper loss of each motor, and P_i is the sum of the iron loss of each motor. P_{out} is given by

$$P_{\mathrm{out}} = 2\sum_{j=f,r}\omega_j T_j. \tag{11}$$

In the modeling of the copper loss P_c, iron loss was neglected for simplicity. Suppose that the magnet torque is much greater than the reluctance torque and that the q-axis current is much greater than the d-axis current; then, the sum of the copper loss of the permanent magnetic motors P_c is expressed as

$$P_c = 2\sum_{j=f,r} R_j i_{qj}^2, \tag{12}$$

where R_j is the armature winding resistance of the motor and i_{qj} is the q-axis current of the motor. Then, the following relationship between the q-axis current and torque is obtained:

$$i_{qj} = \frac{T_j}{K_{tj}} = \frac{T_j}{p_{nj}\Psi_j}, \tag{13}$$

where K_{tj} is the torque coefficient of the motor, p_{nj} is the number of pole pairs, and Ψ_j is the interlinkage magnetic flux. Therefore, the copper loss P_c is given by

$$P_c = 2\sum_{j=f,r}\frac{R_j T_j^2}{K_{tj}^2}. \tag{14}$$

In this study, the equivalent circuit model [19] was used to examine the iron loss. Fig. 7 shows the d- and q-axis equivalent circuits of the permanent magnetic motor.

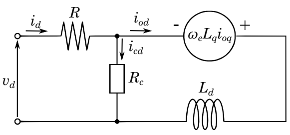

(a) d-axis. (b) q-axis.

Fig. 7. Equivalent circuit of PMSM.

From the circuits, the sum of iron loss P_i is expressed as

$$P_i = 2 \sum_{j=f,r} \frac{\omega_{ej}^2}{R_{cj}} \left\{ (L_{dj} i_{odj} + \Psi_j)^2 + (L_{qj} i_{oqj})^2 \right\}, \tag{15}$$

where ω_{ej} is the electrical angular velocity of the motor, R_{cj} is the equivalent iron loss resistance, L_{dj} is the d-axis inductance, L_{qj} is the q-axis inductance, i_{odj} is the difference between the d- and q-axis current i_{dj}, i_{qj} and the d- and q-axis components of the iron loss current i_{cdj}, i_{cqj}, respectively [19]. In (15), the armature reaction of the d-axis $\omega_e L_d i_{od}$ is neglected since it is much smaller than the electromotive force of the magnet $\omega_e \Psi$. In the modeling of the iron loss, ω_{ej} was approximated as $p_{nj} V/r$ for simplicity since the slip ratio of each wheel was small. Under this condition, P_i is approximated by

$$P_i \approx 2 \frac{V^2}{r^2} \sum_{j=f,r} \frac{p_{nj}^2}{R_{cj}} \left\{ \left(\frac{L_{qj}}{K_{tj}} \right)^2 T_j^2 + \Psi_j^2 \right\}. \tag{16}$$

The equivalent iron loss resistance R_{cj} is expressed as

$$\frac{1}{R_{cj}(\omega_{ej})} = \frac{1}{R_{c0j}} + \frac{1}{R'_{c1j} |\omega_{ej}|}. \tag{17}$$

In (17), the first and second terms on the right-hand side represent the eddy current loss and hysteresis loss, respectively [20]. By applying $\omega_{ej} = p_{nj} V/r$, R_{cj} is expressed as $R_{cj}(V)$.

From the above equations, P_{in} is expressed as

$$\begin{aligned} P_{\text{in}} &= P_{\text{out}} + P_c + P_i \\ &= 2 \sum_{j=f,r} \omega_j T_j + 2 \sum_{j=f,r} \frac{R_j T_j^2}{K_{tj}^2} \\ &\quad + 2 \frac{V^2}{r^2} \sum_{j=f,r} \frac{p_{nj}^2}{R_{cj}} \left\{ \left(\frac{L_{qj}}{K_{tj}} \right)^2 T_j^2 + \Psi_j^2 \right\}. \end{aligned} \tag{18}$$

III. Optimization of Front and Rear Driving-Braking Force Distributions

A. Derivation of Optimal Distribution Ratio

The optimal driving-braking force distribution ratio that minimizes the input power of the inverter is derived here. To derive the optimal distribution ratio, the inertia force of each wheel is neglected in (1) because $J_{\omega_j} \dot{\omega}_j \ll r F_j$ under a high μ load. As noted in [21], the denominator of (4) can be approximated to V when $|\lambda_j| \ll 1$. Therefore, T_j and ω_j can be approximated as

$$T_j = r F_j, \tag{19}$$

$$\omega_j = \frac{V}{r}(1 + \lambda_j). \tag{20}$$

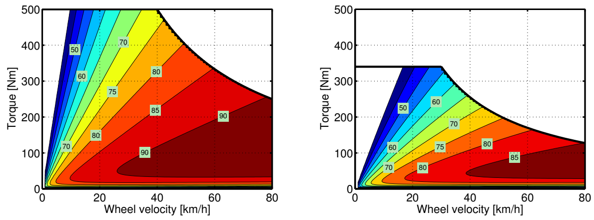

(a) Front motor. (b) Rear motor.

Fig. 8. Motor efficiency (calculated).

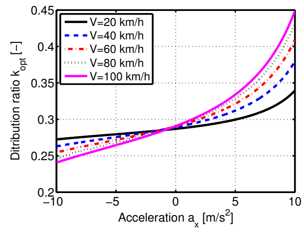

Fig. 9. Optimal distribution ratio k_{opt}.

By applying the above approximation, P_{in} is obtained as $P_{\text{in}}(k)$ [17]. Since $P_{\text{in}}(k)$ is a quadratic function of k, the optimal distribution ratio k_{opt} satisfies $\partial P_{\text{in}} / \partial k |_{k=k_{\text{opt}}} = 0$. Therefore, k_{opt} is derived as a function of V and a_x:

$$k_{\text{opt}}(V, a_x) = \frac{\frac{V}{D'_s N_f(a_x)} + \frac{r^2 R_f}{K_{tf}^2} + \frac{V^2}{R_{cf}(V)} \left(\frac{L_{qf}}{\Psi_f} \right)^2}{\frac{V}{D'_s} \sum_{j=f,r} \frac{1}{N_j(a_x)} + r^2 \sum_{j=f,r} \frac{R_j}{K_{tj}^2} + V^2 \sum_{j=f,r} \frac{1}{R_{cj}(V)} \left(\frac{L_{qj}}{\Psi_j} \right)^2}. \tag{21}$$

B. Numerical Calculation

Fig. 8 shows the calculation results of the experimental vehicle's motor efficiencies when R_{cj} was 300 Ω and R'_{c1f} and R'_{c1r} were 0.13 and 0.053 Ωs/rad, respectively. From Fig. 2 and Fig. 8, the modeling error of the motor efficiency was within ±5% for most evaluated operation areas. Moreover, the front motor had a higher global efficiency than the rear motor because the former can have a much smaller internal diameter than the latter. Therefore, the number of turns of the motor windings and the teeth shape can be optimized for the front motor design.

Fig. 9 shows the calculated k_{opt}. Under a high μ load, the normalized driving stiffness D'_s was set to 12. k_{opt} increased with the acceleration and decreased with increased deceleration. This is mainly because of the influence of the variation in the slip ratio due to load transfer and copper loss. On the other hand, k_{opt} increased with the vehicle velocity. The range of k_{opt} was 0.2–0.45. This is because the front motor had higher efficiency than the rear motor in a wide area of the efficiency map, as shown in Fig. 2.

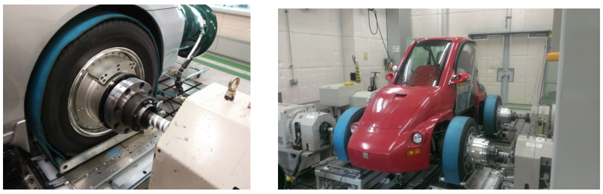

(a) Wheel with bearing. (b) Test vehicle and RC-S.

Fig. 10. Bench test environment.

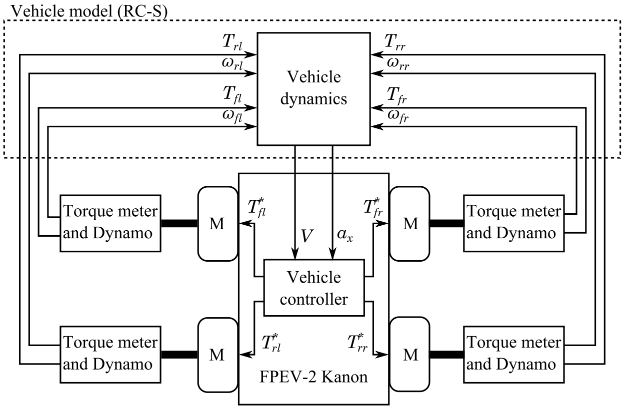

Fig. 11. Block diagram of experiment environment.

IV. Experiment

A. Test Field and Test Bench

A test field for vehicles owned by the National Traffic Safety and Environment Laboratory in Japan was used for the field test. This test field has a 1350 m long straight road, a low μ load, and a slope. This field allows experiments to be performed under various driving conditions. In this study, no-slope and high μ load conditions were employed for the evaluation.

In the bench test, the Real Car Simulation Bench (RC-S) owned by Ono Sokki Co.,Ltd. was used. Fig. 10 shows the bench test environment. In the experiments using RC-S, driving shafts were directly connected to dynamometers through a bearing wheel, which is different from the case of a chassis dynamometer. Fig. 10(a) shows the bearing wheel. By changing the vehicle model of RC-S, experiments can be conducted under various load conditions. In addition, RC-S can control dynamos with a faster response than a chassis dynamometer using rollers, which have greater inertia. Therefore, RC-S is suitable for bench test of electric vehicles driven by motors. In this research, the test bench was very useful because the experiments were not influenced by changes in the wind and load conditions.

Fig. 11 shows the block diagram of the experimental environment using RC-S. The motor torque of each wheel was measured by a torque meter and input to the vehicle model of RC-S. The velocity and acceleration of the vehicle were calculated by vehicle dynamics model in RC-S. In order to control the motors, these values were input to the vehicle controller.

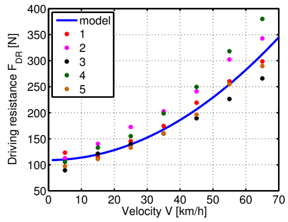

Fig. 12. Comparison of model and measurement results of driving resistance.

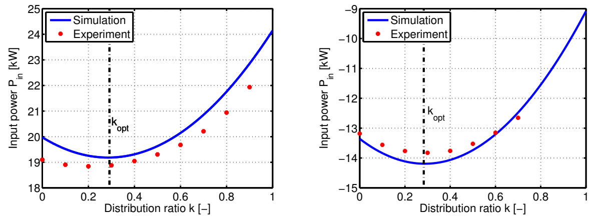

(a) $a_x = 1.5\,\mathrm{m/s^2}$, $V = 40\,\mathrm{km/h}$. (b) $a_x = -2.0\,\mathrm{m/s^2}$, $V = 40\,\mathrm{km/h}$.

Fig. 13. Experimental result of P_{in}.

B. Driving Resistance

For the simulation and bench test, the driving resistance of the test vehicle was measured in the test field. The driving resistance F_{DR} can be determined by

$$F_{\mathrm{DR}}(V) = \mu_0 M g + \frac{1}{2}\rho C_d A V^2, \tag{22}$$

where μ_0 is the rolling friction coefficient, ρ is the air density, C_d is the drag coefficient, and A is the frontal projected area. ρ and A were determined to be $1.205\ \mathrm{kg/m^3}$ and $1.2\ \mathrm{m^2}$, respectively. μ_0 and C_d were 1.28×10^{-2} and 0.863, respectively. These values were obtained empirically. Fig. 12 shows the measured and calculated driving resistance. The measurements were taken five times. As shown in the figure, the model described by (22) matched the measured values.

C. Input Power for Change in Distribution Ratio

Fig. 13 shows the experimental results of P_{in} when the distribution ratio was changed. This experiment was conducted using RC-S. The inverter input power P_{in} can be calculated as

$$P_{\mathrm{in}} = V_{\mathrm{dc}} \sum_{j=f,r} I_{\mathrm{dc}j}, \tag{23}$$

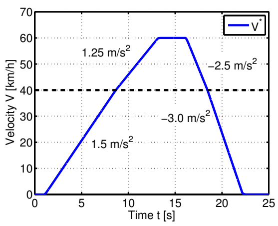

Fig. 14. Reference vehicle speed.

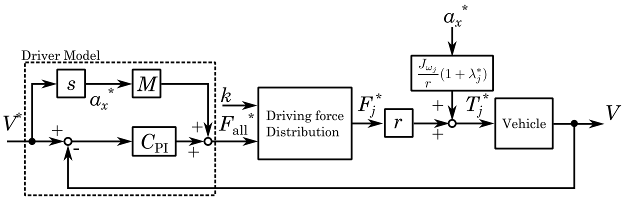

Fig. 15. Vehicle speed control system.

where V_{dc} is the inverter input voltage and I_{dcj} is the front and rear inverter input currents. Fig. 13 shows the results when a_x and V were 1.5 $\mathrm{m/s^2}$ and 40 km/h, respectively, and $-2.0\ \mathrm{m/s^2}$ and 40 km/h, respectively. These conditions were simulated by RC-S. In Fig. 13, the rigid lines represent the calculation results of the computer simulation; here, the approximations presented above were not applied. The value at k_{opt} calculated by (21) is shown as a dashed line. Fig. 13 indicates that P_{in} is a convex function of k. Therefore, a k that minimizes P_{in} exists. In the simulation, although there were errors caused by the approximations of the torque, wheel angular velocity, copper loss, and iron loss, the case of $k = k_{\mathrm{opt}}$ showed almost equal minimum values, as shown in Fig. 13. The experimental results indicate that k_{opt} can mostly minimize the input power, although a little error remains present. Therefore, the approximations assumed in this study were appropriate.

D. Pattern Driving

To demonstrate the effectiveness of the proposed system, the driving cycle was evaluated with both the test field and test bench. Fig. 14 shows the driving cycle, which comprised two-step acceleration, cruising, and two-step deceleration. The accelerations were 1.5 and 1.25 $\mathrm{m/s^2}$, the maximum vehicle speed was 60 km/h, and the decelerations were -2.5 and $-3.0\ \mathrm{m/s^2}$. The cases of $k = 0$, 0.1, 0.2, 0.3, 0.4, 0.5, and k_{opt} were evaluated. In the bench test, the driving resistance was set to the value measured in the field test.

Fig. 15 shows the vehicle velocity control system for determining the vehicle velocity pattern in Fig. 14 during the field test. This system comprised a feedforward controller and a feedback controller. These controllers corresponded to the driver model. The input was the vehicle velocity reference V^*, and the average of all f the wheel velocities was used as the vehicle velocity V in the field test. The value calculated with the vehicle model was used in the bench test. These controllers generated the total reference driving-braking force F_{all}^*. Then, F_{all}^* was distributed to the reference front and rear driving-braking forces F_j^* based on (8) and (9). Represented by the slip ratio, the reference front and rear torques T_j^* are given by

$$T_j^* = rF_j^* + \frac{J_{\omega_j} a_x^*}{r}(1+\lambda_j^*), \tag{24}$$

where the second term of the right-hand side represents the compensation for the inertia torque of the wheels [21]. In order to consider the stability of the vehicle velocity control system, the reference acceleration a_x^* and slip ratio λ_j^* were substituted for their measured values. Because $J_{\omega_j} a_x^*/r$ was much smaller than rF_j^*, the second term did not have a large effect. Therefore, λ_j^* was simply set to 0.05, 0, and -0.05 during acceleration, cruising, and deceleration, respectively.

The vehicle velocity controller $C_{\mathrm{PI}}(s)$ was a proportional-integral (PI) controller that was designed by the pole placement method. The plant of the vehicle velocity controller is given by

$$\frac{V}{F_{\mathrm{all}}} = \frac{1}{Ms}. \tag{25}$$

The pole of vehicle velocity controller was set to -5 rad/s.

Fig. 16 shows the vehicle speed control system for the experiments using RC-S. The inverters and motors of the real vehicle and vehicle model in RC-S represent the actual vehicle plant in Fig. 15. The vehicle model comprised the equations given in section 2.

Fig. 17 shows the experimental results for the vehicle motion in the field and bench tests; the results of each test when $k = k_{\mathrm{opt}}$ are shown. Fig. 17(a) shows the vehicle velocity. In each test, the vehicle velocity followed the reference, similar to the simulation results. This figure also shows the distribution ratio. The optimal distribution ratio k_{opt} increased during acceleration and decreased during deceleration. This result matched the previous calculations. Fig. 17(c) and Fig. 17(d) show the front and rear driving-braking forces, respectively. The total driving-braking force F_{all} was distributed based on k. In addition, the absolute values of the driving force in the simulation and bench test were equal to that of the field test. Therefore, the driving resistance model was appropriate, and the test bench realized the same load as the field test.

Fig. 18 shows the energy consumption in each experimental test. The energy consumptions during acceleration, cruising, and deceleration are shown separately. In order to confirm the reproducibility of the experimental results, the average values and standard deviations, shown as error bars, were calculated for the field and bench tests, which were carried out 12 and 8 times, respectively. In the computer simulation and RC-S, the energy consumption and regenerated energy during each driving section were minimized and maximized by the proposed system. In the field test, the effectiveness of the proposed system with regard to the total energy consumption was not clear because of the large dispersion for the data. However, Fig. 18(a) and Fig. 18(e) clearly show the effectiveness in the case of large acceleration because the variations in the wind and load conditions on the energy consumption was relatively small with a large torque. In the computer simulation results, the high-speed operation showed worse efficiency than the experimental results. This is because the simulation model had greater iron loss than the actual values. A comparison of the simulation and two tests showed that their energy consumptions roughly agreed. Thus, the proposed system achieved 9 % and 8 %

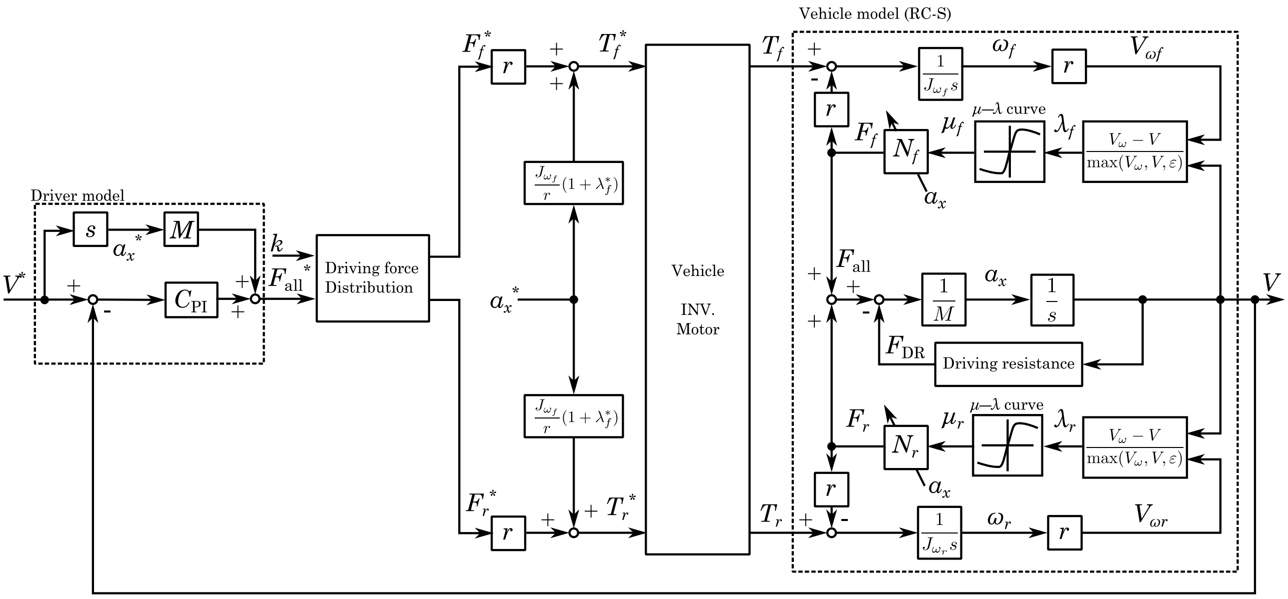

Fig. 16. Vehicle speed control system and vehicle model of RC-S.

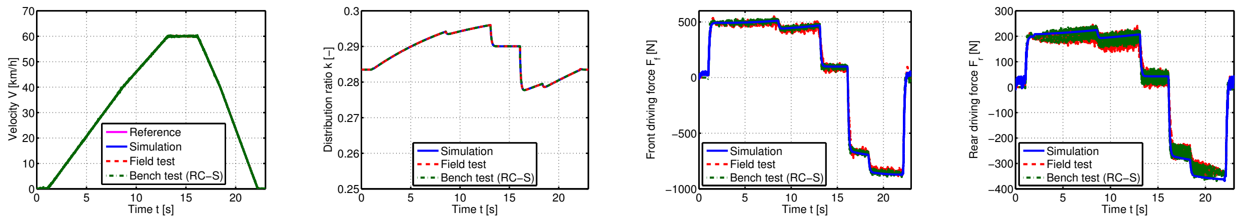

(a) Velocity. (b) Distribution ratio. (c) Front driving force. (d) Rear driving force.

Fig. 17. Experimental results related to vehicle motion of driving pattern ($k = k_{\rm opt}$).

decreases in the energy consumption during the bench and field tests, respectively, compared with $k = 0.5$.

V. Conclusion

This paper proposes a model-based range extension control system for electric vehicles that optimizes the front and rear driving-braking force distributions. The slip ratio of the wheels and the copper and iron losses of the motors are considered to minimize the energy consumption. Because the proposed distribution method depends on only the vehicle acceleration and velocity, the distribution ratios during the acceleration or deceleration processes can be optimized.

A bench test was carried out to realize results with high reproducibility. The results of a computer simulation, actual field test, and bench test were compared. The simulation and experimental results confirmed the effectiveness of the proposed system. The simulation and bench test results on the energy consumption matched the field test results.

Therefore, this study verified that the proposed system can extend the cruising range of electric vehicles and accurately measure the energy consumption.

Acknowledgment

This research was partly supported by the Industrial Technology Research Grant Program from the New Energy and Industrial Technology Development Organization(NEDO) of Japan (No. 05A48701d) and by a grant from the Ministry of Education, Culture, Sports, Science and Technology (No. 22246057).

References

[1] Y. Hori: “Future Vehicle Driven by Electricity and Control—Research on Four-Wheel-Motored: “UOT Electric March II””, IEEE Trans. IE, Vol. 51, No. 5, pp. 954–962 (2004)

[2] K. Maeda, H. Fujimoto, and Y. Hori: “Four-Wheel Driving-Force Distribution Method Based on Driving Stiffness and Slip Ratio Estimation for Electric Vehicle with In-Wheel Motors”, 8th IEEE Vehicle Power and Propulsion Conference, pp. 1286–1291 (2012)

[3] T. Hsiao: “Robust Estimation and Control of Tire Traction Forces”, IEEE Trans. Veh. Technol., Vol. 62, No. 3, pp. 1378–1383 (2013)

[4] J. Kang, J. Yoo, and K. Yi: “Driving Control Algorithm for Maneuverability, Lateral Stability, and Rollover Prevention of 4WD Electric Vehicles with Independently Driven Front and Rear Wheels”, IEEE Trans. Veh. Technol., Vol. 60, No.7, pp. 2987–3001 (2011)

[5] K. Nam, H. Fujimoto, and Y. Hori: “Advanced Motion Control of Electric Vehicles Based on Robust Lateral Tire Force Control via Active Front Steering”, IEEE/ASME Trans. Mechatron., Vol. 19, No. 1, pp. 289–299 (2014)

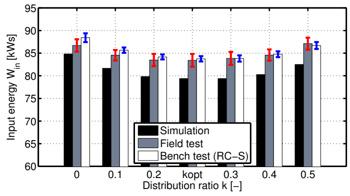

(a) Acceleration 1 (1.5 $\mathrm{m/s^2}$, 0-40 km/h).

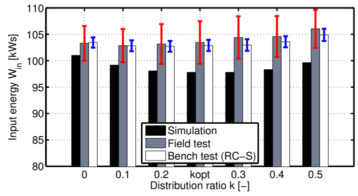

(b) Acceleration 2 (1.25 $\mathrm{m/s^2}$, 40-60 km/h).

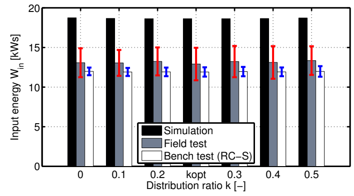

(c) Cruising (60 km/h, 3 s).

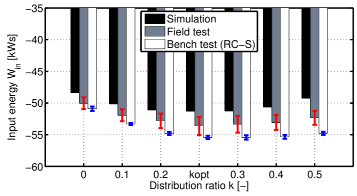

(d) Deceleration 1 ($-2.5\,\mathrm{m/s^2}$, 60-40 km/h).

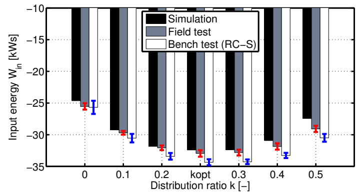

(e) Deceleration 2 ($-3.0\,\mathrm{m/s^2}$, 40-0 km/h).

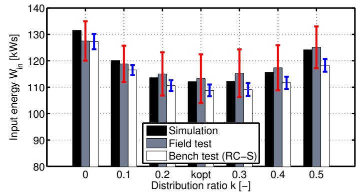

(f) Total.

Fig. 18. Experimental results of pattern driving (comparison of energy consumption).

[6] T. Imura and Y. Hori: "Maximizing Air Gap and Efficiency of Magnetic Resonant Coupling for Wireless Power Transfer Using Equivalent Circuit and Neumann Formula", IEEE Trans. IE, Vol. 58, No. 10, pp. 4746–4752 (2011)

[7] S. Chopa and P. Bauer: "Driving Range Extension of EV With On-Road Contactless Power Transfer—A Case Study", IEEE Trans. IE, Vol. 60, No. 1, pp. 329–338 (2013)

[8] J. Shin, S. Shin, Y. Kim, S. Ahn, S. Lee, G. Jung, S. J. Jeon, and D. H. Cho: "Design and Implementation of Shaped Magnetic-Resonance-Based Wireless Power Transfer System for Roadway-Powered Moving Electric Vehicles", IEEE Trans. IE, Vol. 61, No. 3, pp. 1179–1192 (2014)

[9] P. J. Grbovic, P. Delarue, P. L. Moigne, and P. Bartholomeus: "The Ultracapacitor-Based Regenerative Controlled Electric Drives with Power-Smoothing Capability", IEEE Trans. IE, Vol. 59, No. 12, pp. 4511–4522 (2012)

[10] J. Cao and A. Emadi: "A New Battery/UltraCapacitor Hybrid Energy Storage System for Electric, Hybrid, and Plug-In Hybrid Electric Vehicles", IEEE Trans. Power Electron., Vol. 27, No. 1 pp. 122–132 (2014)

[11] M. Montazeri, M. Soleymani, and S. Hashemi: "Impact of Traffic Conditions on the Active Suspension Energy Regeneration in Hybrid Electric Vehicles", IEEE Trans. IE, Vol. 60, No. 10, pp. 4546–4553 (2013)

[12] H. Toda, Y. Oda, M. Kohno, M. Ishida, and Y. Zaizen: "A New High Flux Density Non-Oriented Electrical Steel Sheet and Its Motor Performance", IEEE Trans. Magn., Vol. 48, No. 11, pp. 3060–3063 (2012)

[13] K. Inoue, K. Kotera, Y. Asano, and T. Kato: "Optimal Torque and Rotating Speed Trajectories Minimizing Energy Loss of Induction Motor under Both Torque and Speed Limits", in Proc. Power Electronics and Drive Systems, 2013 IEEE 10th International Conference, pp. 1127–1132 (2013)

[14] X. Yuan and J. Wang: "Torque Distribution Strategy for a Front- and Rear-Wheel-Driven Electric Vehicle", IEEE Trans. Veh. Technol., Vol. 61, No. 8, pp. 3365–3374 (2012)

[15] H. Fujimoto and H. Sumiya: "Range Extension Control System of Electric Vehicle Based on Optimal Torque Distribution and Cornering Resistance Minimization", in Proc. 37th Annual Conference of the IEEE Industrial Electronics Society, pp. 3727–3732 (2011)

[16] H. Fujimoto, S. Egami, J. Saito, and K. Handa: "Range Extension Control System for Electric Vehicle Based on Searching Algorithm of Optimal Front and Rear Driving Force Distribution", in Proc. 38th Annual Conference of the IEEE Industrial Electronics Society, pp. 4244–4249 (2012)

[17] S. Harada and H. Fujimoto: "Range Extension Control System for Electric Vehicle on Acceleration and Deceleration Based on Front and Rear Driving/Braking Force Distribution Considering Slip Ratio and Motor Loss", in Proc. 39th Annual Conference of the IEEE Industrial Electronics Society, Vienna, Austria, pp. 6624–6629 (2013)

[18] H. B. Pacejka and E. Bakker: "The Magic Formula Tyre Model", Vehicle System Dynamics: International Journal of Vehicle Mechanics and Mobility , Vol. 21, No. 1, pp. 1–18 (1992)

[19] S. Morimoto, Y. Tong, Y. Takeda, and T. Hirasa: "Loss Minimization Control of Permanent Magnet Synchronous Motor Drives", IEEE Trans. IE, Vol. 41, No. 5, pp. 511–517 (1994)

[20] C. Kaido: "Effects of Cores on the Characteristics of an Induction VCM", IEEE Trans. Magnetics in Japan, Vol. 9, No. 6, pp. 110–116 (1994)

[21] H. Fujimoto, J. Amada, and K. Maeda: "Review of Traction and Braking Control for Electric Vehicle", in Proc. The 8th IEEE Vehicle Power and Propulsion Conference, Seoul, Korea, pp. 1292–1299 (2012)